Tuijin Jishu/Journal of Propulsion Technology
ISSN: 1001-4055
Vol. 45 No. 1 (2024)

Piezoelectric MEMS-Based Underwater Acoustic Vector Sensor: Design and Characterization

Gauri Varade[1], Liladhar Bhamare[1], Hrishikesh Mehta[2], and Nikita Mitra[1]

[1]Research Centre, Department of Electronics & Telecommunication Engineering, Oriental University, Indore, India

[2]Research & Development, Aethertec Innovative Solutions, Pune, India

Abstract: **-** This study introduces a novel microfabrication approach for developing a directional hydrophone with a distinctive design incorporating cross-shaped piezoelectric cantilevers. In the microfabrication process, a thin layer of aluminum nitride (AlN), featuring Molybdenum (Mo) thin film electrodes, is utilized as the piezoelectric functional layer for a cantilever-based underwater ultrasonic microelectromechanical system (MEMS) hydrophone. Through parameterized simulation, the length of the cantilevers is systematically adjusted within the range of 100 to 1000 µm to achieve the first resonant mode within the 20 kHz to 200 kHz frequency spectrum, aligning with the targeted underwater ultrasonic acoustic frequencies. The microsystem design incorporates cantilevers arranged in a cross configuration, aiming to realize a unique MEMS hydrophone with omnidirectional response capabilities. To investigate the first resonance frequency mode and displacement measurements, a Laser Doppler Vibrometer is employed, demonstrating a robust correlation between simulation predictions and experimental data. In-water responsivity and directionality assessments of the piezoelectric MEMS cantilevers reveal a maximum sensitivity of up to -153 dB, accompanied by an omnidirectional directivity pattern achieved by the fabricated MEMS sensor.

Keywords*: MEMS, piezoelectricity, hydrophone, sensitivity, stress, underwater acoustic vector, sensor*

1. Introduction

The hydrophone, a pivotal component in ocean exploration, military operations, underwater sound monitoring, and sonar systems, functions as a crucial radio receiver [1]. Leveraging Microelectromechanical Systems (MEMS) technology, an interdisciplinary integration of physics, mechanics, acoustics, and electronics [2], hydrophones are designed and produced to capture underwater sounds effectively. MEMS-based hydrophones, operating as electroacoustic transducers, employ piezoelectric technology to convert high sound pressure mechanical impulses into electrical signals. Commonly utilizing piezoelectric or piezo-resistive materials [3-5], these MEMS sensors have demonstrated precision in locating and discerning the direction of underwater noise, earning recognition as pioneering directional hydro-acoustic sensors in 1996 [6]. Over time, they have gained widespread application in various underwater scenarios, particularly in sonar systems.

An intriguing facet of MEMS-based hydrophone development involves biomimetic technology, drawing inspiration from natural phenomena to create innovative hydrophones [7]. Notable examples include T-shaped vector hydrophones inspired by fish lines, employing piezoresistive cantilevers [8]. Classified as the "8" dipole type, these hydrophones exhibit remarkable sensitivity, measuring -180 dB and -192 dB at 1 kHz. Some hydrophones incorporate liquid models to record the gap between piezoresistive cantilevers and the surrounding wall, demonstrating effectiveness in capturing underwater sounds within the frequency range of 100 Hz to 8 kHz

[9]. Additionally, a micro machined hydrophone utilizing a piezoelectric PZT film has been developed, employing reverse wind techniques to enhance sensitivity [10].

Significant strides have been achieved in the realm of piezoelectric micro machined sensors in recent years. Devices rooted in aluminum nitride (AlN) MEMS, such as microphones [11], piezoelectric micro machined ultrasonic transducers (pMUTs) [12], inertial sensors [13], and radio frequency resonance devices [14], are poised to gain wider prominence. The appeal of AlN lies in its compatibility with CMOS manufacturing processes, biocompatibility, and low energy consumption. Despite its relatively low piezoelectric coefficient [15], the small dielectric constant of AlN [30] renders it highly attractive for piezoelectric MEMS transducers.

While piezoelectric-based hydrophones exhibit excellent performance within the necessary ultrasonic range [16], their physical size imposes constraints on current sonar systems [17]. Consequently, recent attention has shifted towards the miniaturization of hydrophones, with potential advantages including stable operation, high precision, low cost, and increased efficiency. The reduction in size of MEMS hydrophones offers the benefit of enhanced measurement accuracy, as they are less susceptible to acoustic diffraction [18].

In recent advancements, the integration of piezoelectric cantilevers into hydroacoustic sensing has been instrumental in enhancing the directional sensitivity of hydrophones [19]. This improvement involves incorporating additional layers onto the cantilever through the alignment of parallel films, creating a stress layer that allows stress to "bend in plane" [20]. Notably, the sensitivity of the mechanical mechanism to underwater sound is heightened by stress gradients during assembly and disassembly, facilitating the definition of structures. Nitride materials, with a particular emphasis on aluminum nitride, are commonly employed in the cantilever process, enabling the formation of curved cantilevers.

These micromechanical systems exhibit increased sensitivity to deformations induced by external mechanical stimuli [21-25], thereby enhancing the ability to control direction and subsequently detect noise. Out-of-plane curved cantilevers prove especially advantageous as a foundation for steering hydrophones. A well-configured assembly, involving the installation of four curved consoles and appropriate signal processing, facilitates the creation of a directional structure that augments underwater sound directivity. This innovative approach, leveraging new and more efficient methods, enables the development of advanced data collection techniques for acquiring long-term information about ocean acoustics [26-30].

Among marine inhabitants, dolphins and whales utilize short ultrasonic pulses for environmental perception, communication, and habitat exploration [31-33]. The recording, analysis, and processing of acoustic data serve as pivotal tools for enhancing the tracking capabilities of dolphins in their natural settings. In the context of this study, an acoustic directional receiver was developed using a generator based on a transverse configuration of four out-of-plane twisted piezoelectric cantilever beams. Finite Element Method (FEM) simulations were conducted to explore the resonance behavior of the system. The resulting crossover configuration exhibited a directional response, enabling the detection of sound direction in water.

This research unfolds in three distinct parts, each making significant contributions to the advancement of hydroacoustic technology. Firstly, it presents the final design and analysis of the micro cantilever structure. Secondly, it introduces the Micro-Electro-Mechanical Systems (MEMS) design process. Lastly, the study characterizes the sensitivity and fidelity of the hydrophone, marking a notable milestone as the first directional hydrophone based on piezoelectric cantilevers designed for underwater ultrasonic communication in the frequency range of 20 kHz to 200 kHz. The incorporation of a novel algorithm challenges previously underexplored aspects of input experiences in hydroacoustic studies.

2. Materials and Methods

In the pursuit of designing and fabricating devices, a pivotal aspect involves harnessing piezoelectricity—a coupling mechanism that intricately links the mechanical and electrical characteristics of a material. This phenomenon is characterized by the generation of an electrical charge in response to mechanical deformation and, conversely, mechanical deformation occurring when an electrical charge is applied to the material. The

foundational mathematical expressions governing this coupling, referred to as piezoelectric constitutive equations or "coupled equations," are provided in the stress-charge form and can be found in the literature [32].

$$T=sES-eTE \quad (1)$$

$$D=eS+\varepsilon E \quad (2)$$

In this context, the variables are defined as follows: S represents the strain tensor, sE denotes the elasticity matrix, T stands for the stress tensor, e is the piezoelectric coupling matrix, D signifies the tensor of electric displacement, ε represents the electrical permittivity, and E represents the electric field.

The investigation of MEMS directional hydrophones, with a focus on nitride materials and the optimization of receiving sensitivity across a specific frequency range, involved a meticulous design and simulation process using the finite element method implemented through COMSOL Multiphysics. The transducer design included simulations of acoustics-structure interaction and piezoelectric effects in a water environment, as illustrated in Figure 1. The approach of anchoring one end of the cantilever while leaving all other faces unconstrained allowed for controlled device bending. The mesh employed consisted of 202,168 elements, utilizing free quad and free tetrahedral finite elements for an accurate representation.

Two distinct structures were simulated, both incorporating a piezoelectric aluminum nitride (AlN) functional layer. The thicknesses of these layers were set at 1 µm and 2 µm, resulting in flexural stiffness values of approximately 3×10^{-11} Nm^2 and 9×10^{-11} Nm^2, respectively. It's noteworthy that a higher thickness of AlN contributed to increased flexural stiffness, making the cantilever less responsive and more brittle. The chosen piezoelectric coefficients for AlN were $e_{13}=-0.58$C m^{-2} and $e_{33}=1.55$C m^{-2}, and 200 nm thick top and bottom molybdenum (Mo) electrodes were implemented. To mitigate short circuits in water, a perylene conformal coating with a thickness of 1 µm was applied. The mechanical properties of the materials, along with their respective thicknesses, crucial for designing and simulating the micro cantilever's response, are outlined in Table 1.

This comprehensive approach ensures the accuracy and reliability of the experimental setup, considering various factors such as material properties, geometry, and environmental conditions. The detailed description provides a clear understanding of the methodology employed in the design and simulation of the stress-driven device structure for MEMS directional hydrophones.

3. Simulation in COMSOL

3.1 Model Development

The unit system is integrated using global system (SI) units in the model development. The geometry shape function is automated, and the formation of inverted elements is prevented by curving interior domain elements. The spatial and material frame coordinates are denoted as x-, y-, and z-axes, respectively. The geometry and mesh frame coordinates are represented by Xg-, Yg-, and Zg-Axes; Xm-, Ym-, and Zm-Axes, respectively. The primary coordinate names are t1, t2, and n. The geometric characteristics are detailed in Table 1.

Table 1. Geometry Statistics

Description	Value
Space dimension	3
Number of domains	6
Number of boundaries	36
Number of edges	72
Number of vertices	44

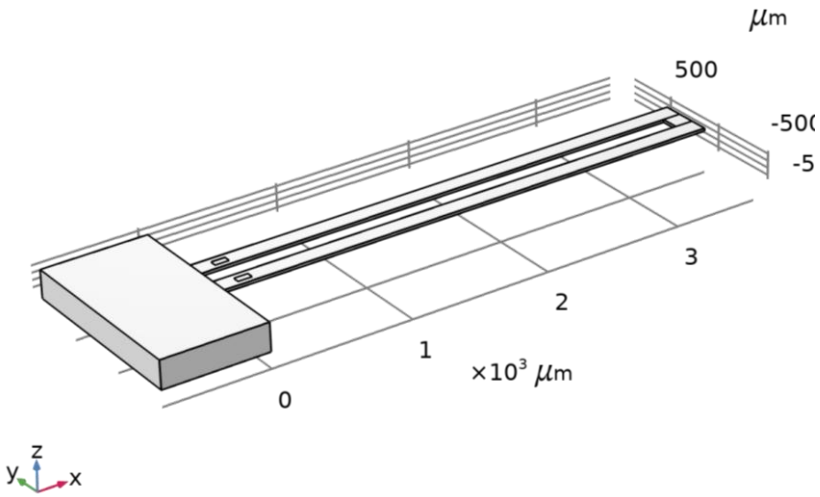

Figure 1. Ultrasonic sensor for detection of speed bumps and potholes [18]

The block 1, at initial conditions of sensor positioning the {x, y, z} = {0, 0, 0} the axis type is valued by z-axis. The size and shape are width = 3600 μm, depth = 130 μm and height = 20 μm, respectively. The block 2 is positioned {x, y, z} = {0, 260, 0} valued by z-axis and is constructed similar to block 1. The block 3 is positioned {x, y, z} = {3470, 130, 0} at z-axis the size and shape are width = 130 μm, depth = 130 μm and height = 20 μm, respectively. Subsequently, the block 4 is positioned {x, y, z} = {120, 40, 19.6}, at z-axis the size and shape are width = 100 μm, depth = 50 μm and height = 0.4 μm, respectively. The block 5 is positioned {x, y, z} = {120, 300, 19.6}, at z-axis with similar size and shape of width = 100 μm, depth = 50 μm and height = 0.4 μm, respectively is applied. The block 6 is positioned at {x, y, z} = {-750, 500, -180}, at z-axis with size of width = 750 μm, depth = 1390 μm and height = 200 μm, respectively.

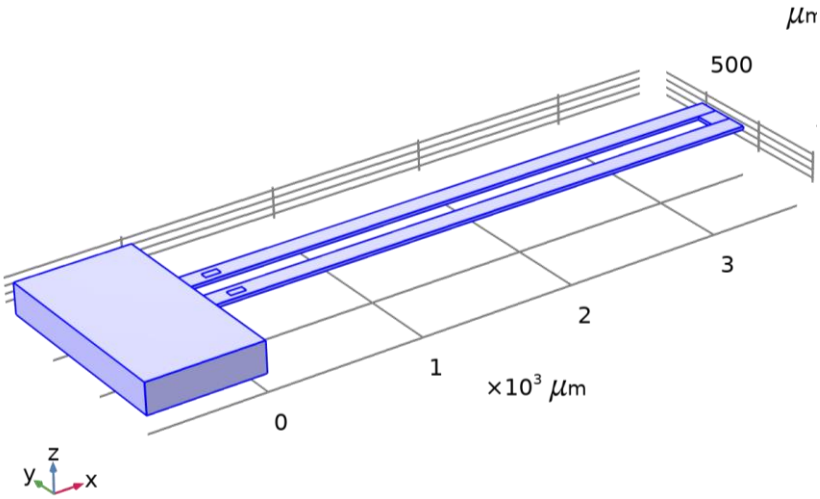

Figure 2. Silicon based material project of the piezoelectric MEMS based underwater acoustic vector sensor

From the Figure 2, the material density is valued 2329 kg/m^3. The Table 2 describes applied parameters on the sensor.

Table 2. Basic Parameters

Description	Value
Relative permeability	{{1, 0, 0}, {0, 1, 0}, {0, 0, 1}}
Electrical conductivity	{{$1e^{-12}$ S/m, 0, 0}, {0, $1e^{-12}$ S/m, 0}, {0, 0, $1e^{-12}$ S/m}}
Coefficient of thermal expansion	{{$2.6e^{-6}$ 1/K, 0, 0}, {0, $2.6e^{-6}$ 1/K, 0}, {0, 0, $2.6e^{-6}$ 1/K}}
Heat capacity at constant pressure	700 J/(kg*K)
Relative permittivity	{{11.7, 0, 0}, {0, 11.7, 0}, {0, 0, 11.7}}
Density	2329 kg/m^3
Thermal conductivity	{{130 W/(m*K), 0, 0}, {0, 130 W/(m*K), 0}, {0, 0, 130 W/(m*K)}}
Young's modulus	$170e^9$ Pa
Poisson's ratio	0.28
Refractive index, real part	{{3.48, 0, 0}, {0, 3.48, 0}, {0, 0, 3.48}}
Refractive index, imaginary part	{{0, 0, 0}, {0, 0, 0}, {0, 0, 0}}

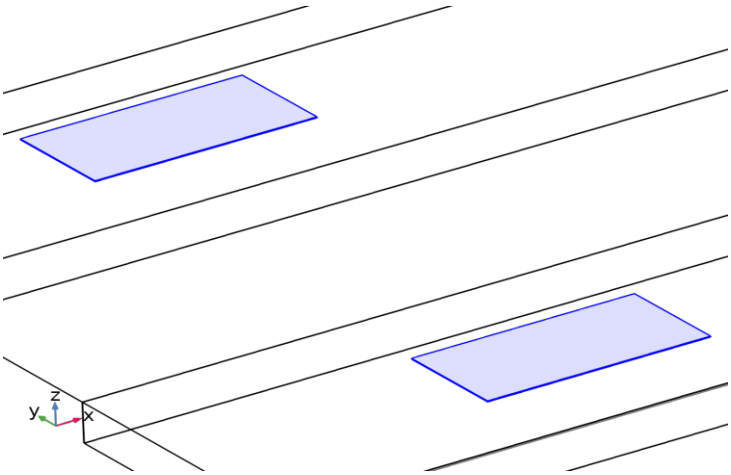

Figure 3. p-type Silicon (single-crystal, lightly doped)

The p-type silicon (single-crystal, lightly doped) geometry is illustrated in Figure 3. The material parameter is described in Table 3.

Table 3. Material Parameters

Name	Value	Unit
Density	2330 kg/m^3	kg/m^3
Relative permittivity	{{4.5, 0, 0}, {0, 4.5, 0}, {0, 0, 4.5}}	1
Electrical conductivity	1×10^{-12}	S/m

Various anisotropic and Voigt notations consisting elasticity matrix and loss factor for elasticity is included. The piezo-resistance and elasto-resistive coupling matrix, is considered in COMSOL Multiphysics software environment. From Figure 2. The piezo-resistivity at domain currents is calculated using traditional equations as,

$$\nabla \cdot J = Q_j \quad (3)$$

$$J = \sigma E + J_e \quad (4)$$

$$E = -\nabla \cdot \mathrm{V} \quad (5)$$

By keeping the displacement and electric potential as quadratic value with manual terminal sweep off and reference impedance at 50\Omega various variables are selected with expression and selective boundaries.

As per Figure 2, the linear elastic material is quantified using the following traditional equations,

$$-\nabla \cdot \sigma = \mathrm{F_v}, \sigma = s \quad (6)$$

$$s - S_0 = C : (\epsilon - \epsilon_0 - \epsilon_{inlet}) \quad (7)$$

$$\epsilon = \frac{1}{2}[(\nabla \cdot \mathrm{u})^T + \nabla u] \quad (8)$$

From Figure 3, the electric insulation is calculated as $-\mathrm{n} \cdot \mathrm{J} = 0$.

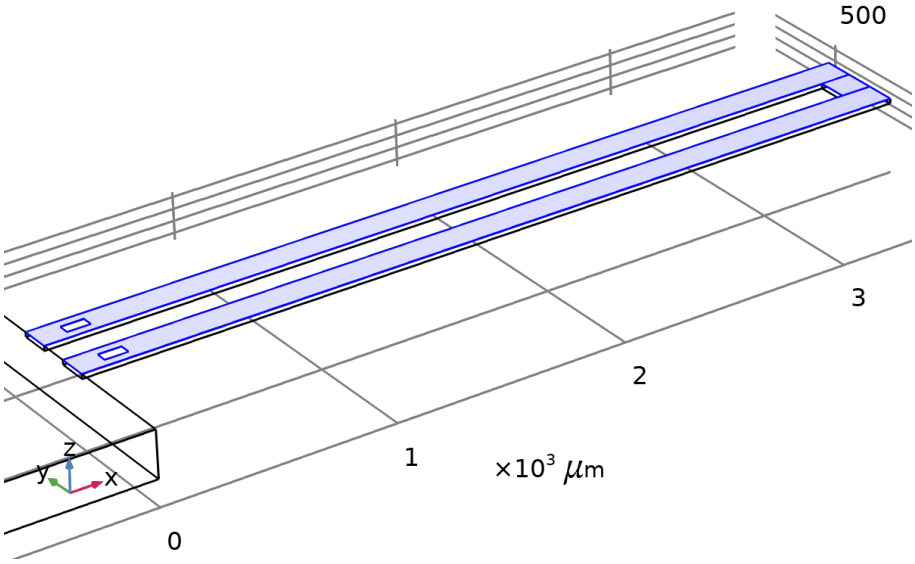

Figure 4. Calculation of load boundary

The calculations of load boundary are referred from the equations with pressure rate of 1 Pa as stated below

$$\sigma \cdot n = F_A \quad (9)$$

$$F_A = -p \cdot n \quad (10)$$

The piezoelectric material from Figure 3 can be calculated using the following equations as,

$$\nabla \cdot \mathrm{J} = \mathrm{Q_j} \quad (11)$$

$$J = \sigma_{c,eff} \cdot E + J_e \quad (12)$$

$$\sigma_{c,eff} = (\sigma_c^{-1} + \Delta\rho)^{-1} \quad (13)$$

$$\Delta\rho = \pi_l \cdot J \cdot \sigma \quad (14)$$

$$E = -\nabla \cdot V \quad (15)$$

The temperature is kept constant at 293.15k and the dopant density is 4.525e18 cm^3.

The fixed geometric constraints are calculated as shown in Figure 5, based on the testing parameters like u, v and w. The elemental analysis is incorporated to understand the statistical mesh patterns as illustrated in Figure 6. The mesh statistics is described in Table 4.

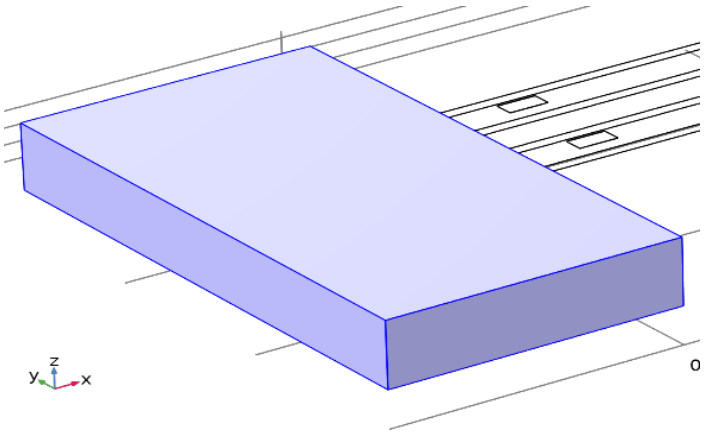

Figure 5. Fixed geometric constraints

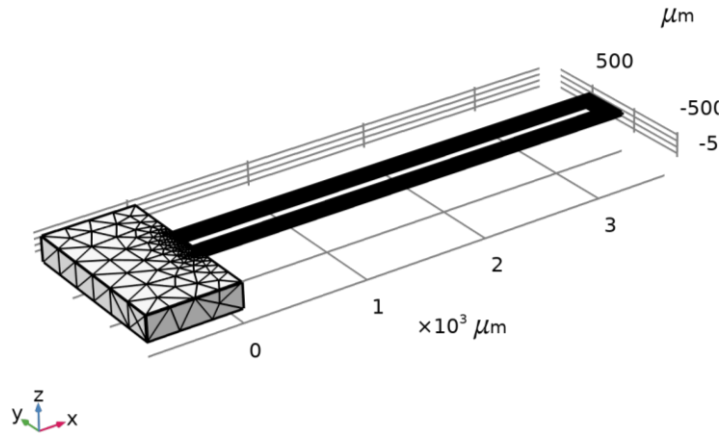

Figure 6. Mesh analysis of the piezoelectric MEMS based underwater acoustic vector sensor

Table 4. Mesh Statistics

Description	Value
Minimum element quality	$1.273E^{-5}$
Average element quality	0.6611
Tetrahedron	31069
Triangle	10910
Edge element	1452
Vertex element	44
Maximum element size	239
Minimum element size	17.4
Curvature factor	0.4
Resolution of narrow regions	0.7
Maximum element growth rate	1.4

Predefined size	Finer

4. Results and Discussions

The computational study of the piezoelectric MEMS-based underwater acoustic vector sensor is conducted based on the compiled equations described in Section 3 and dependent variables within the defined water-based constraints. At a relative tolerance of 0.0010 and a pivoted threshold of 0.1, the factor in error estimation is 400. Various variables such as the displacement field, electric potential, and conjugate gradients of the solver are segregated to imply the results. The interactive dataset of the solution is evaluated and described in Figure 7 and Table 5.

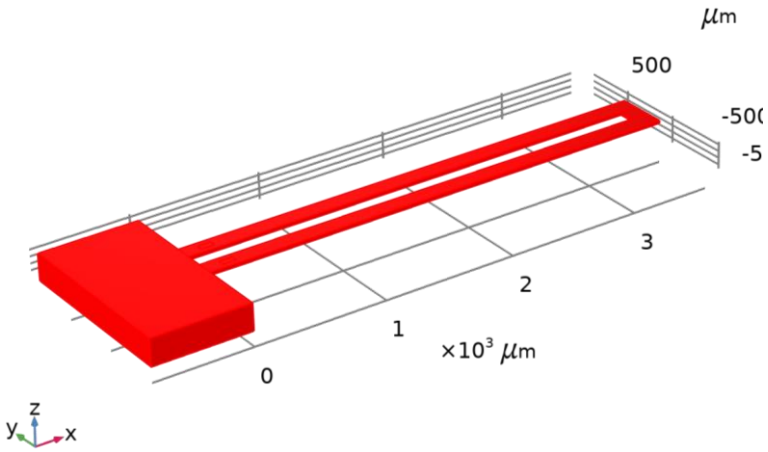

Figure 7. Interactive 3D evaluation of the piezoelectric MEMS based underwater acoustic vector sensor

Table 5. Interactive 3D Values

x	y	z	Value
3599.8	184.67	-177.93	0.25145
3523.0	86.654	-172.26	0.24425
3600.5	200.97	-177.98	0.25152
3600.5	167.98	-177.98	0.25152
3599.7	188.65	-177.93	0.25145
3598.8	185.25	-177.86	0.25136
3598.9	192.90	20.000	0.0000
3599.5	3.1686	20.000	0.0000
3599.6	-2.2737E-13	19.968	0.0000
3599.9	0.15355	20.000	0.0000
3600.5	0.49795	-177.98	0.25151
3600.4	0.86377	-177.98	0.25151
3597.8	0.32392	-177.78	0.25126
3596.2	1.2890	-177.66	0.25111

x	y	z	Value
3597.2	1.0341	-177.74	0.25121
3597.9	0.25448	-177.79	0.25128
3598.4	-8.2091E-7	-177.84	0.25132
3599.7	0.61567	-177.92	0.25144
3599.1	-1.0604E-6	-177.93	0.25139
3599.4	0.45568	-177.90	0.25141

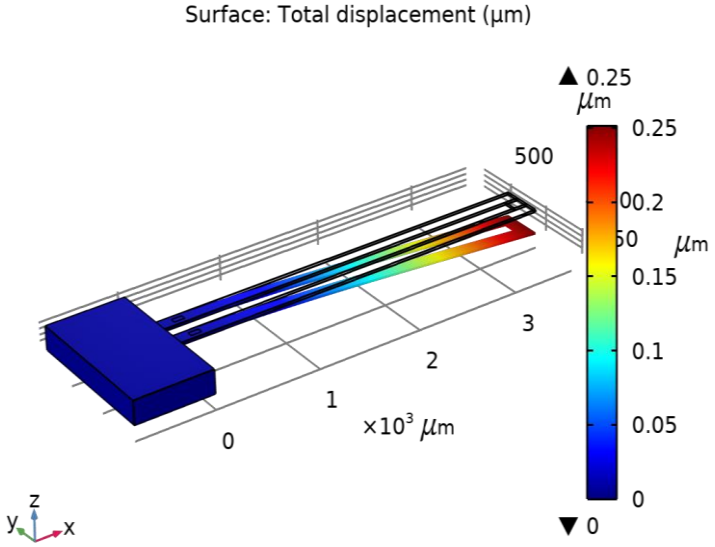

Figure 8. Total displacement of the piezoelectric MEMS based underwater acoustic vector sensor

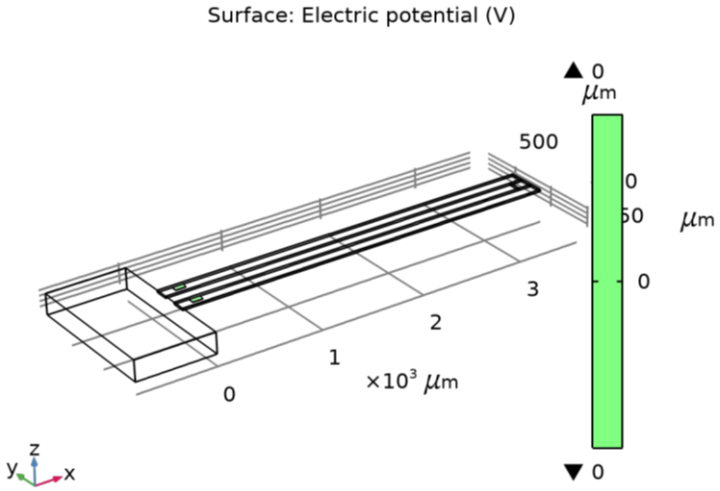

Figure 9. Surface electric potential (V) of the piezoelectric MEMS based underwater acoustic vector sensor

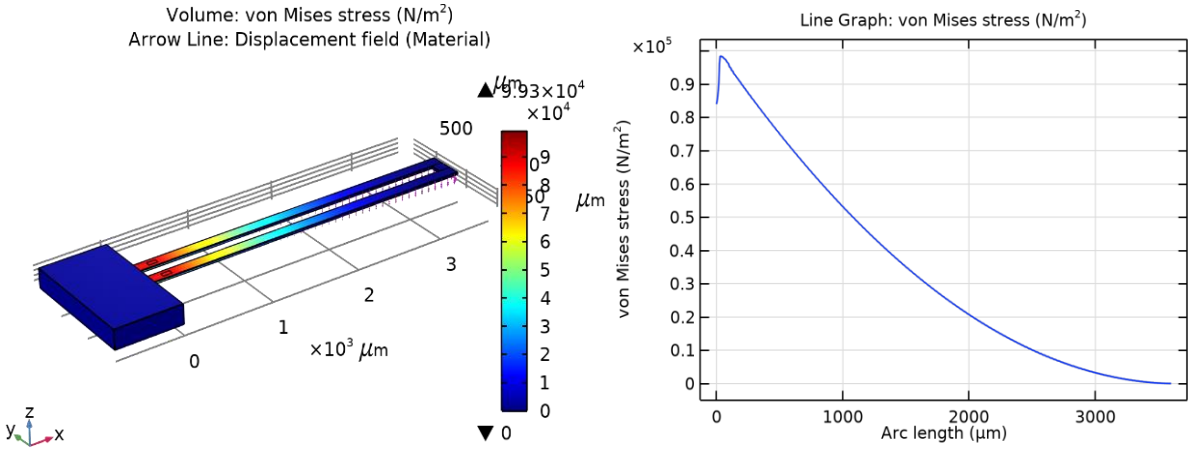

Figure 10. The von mises stress (N/m²) with arrow line of displacement field and the line graph of the material with respect to arc length (μm)

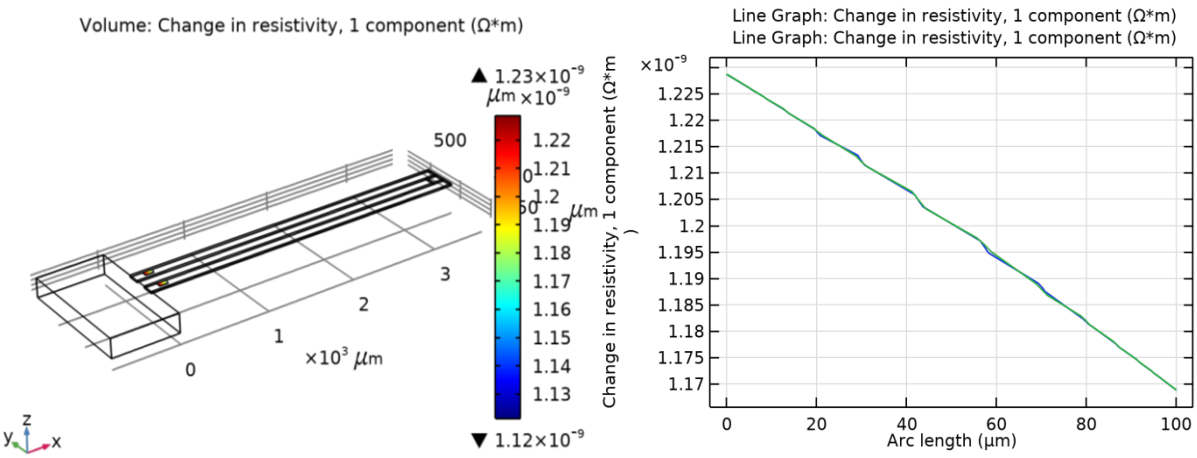

Figure 11. Volume and line graph of change in resistivity of electrical component in Ω × m with respect to arc length (μm)

The total displacement of the piezoelectric MEMS-based underwater acoustic vector sensor is illustrated in Figure 8. Stress and strain analysis were performed to determine the relationship between voltage and sound pressure waves. The surface electric potential (V) of the piezoelectric MEMS-based underwater acoustic vector sensor is shown in Figure 9. From Figures 10 and 11, the von Mises stress with line response and volume change in resistivity with the line response are evaluated concerning the change in arc length, respectively. It is observed that the change in stress corresponds to the change in sensor resistivity.

5. Conclusion

In conclusion, the amalgamation of Micro-Electro-Mechanical Systems (MEMS) technology with piezoelectric materials stands as a groundbreaking avenue propelling the evolution of underwater acoustic sensors. This synergistic partnership has yielded a new generation of sensors characterized by compactness, energy efficiency, and exceptional performance, surpassing the sensitivity and directionality of traditional hydrophones or accelerometer-based counterparts. The in-depth exploration conducted in this study delves into the intricate design and analysis of a piezoelectric MEMS-based underwater acoustic vector sensor, clearly demonstrating its viability and effectiveness in detecting underwater acoustic signals.

The intersection of MEMS and piezoelectricity not only promises enhanced sensor capabilities but also paves the way for innovative solutions in underwater acoustic sensing. The findings presented herein underscore the need for continued research and development to bridge the gap between theoretical advancements and the practical

implementation of hardware sensors. This ongoing exploration lays a solid foundation for the potential evolution of piezoelectric MEMS-based underwater acoustic vector sensors, positioning them as a transformative alternative in the landscape of underwater sensing technologies. As technology progresses, these sensors may play a pivotal role in reshaping our understanding and utilization of underwater acoustic data, opening new horizons for applications in marine research, environmental monitoring, and defense.

References

[1] M. Shirvanimoghaddam, M. M. Abolhasani, M. Farhangi, V. Z. Barsari, H. Liu, M. Dohler, and M. Naebe, "Towards a Green and Self-Powered Internet of Things Using Piezoelectric Energy Harvesting," IEEE Access, vol. 7, pp. 94533–94556, 2019.

[2] S. S. Won, H. Seo, M. Kawahara, S. Glinsek, J. Lee, Y. Kim, C. K. Jeong, A. I. Kingon, and S. H. Kim, "Flexible Vibrational Energy Harvesting Devices Using Strain-Engineered Perovskite Piezoelectric Thin Films," Nano Energy, vol. 55, pp. 182–192, 2019.

[3] F. Ali, W. Raza, X. Li, H. Gul, and K. H. Kim, "Piezoelectric Energy Harvesters for Biomedical Applications," Nano Energy, vol. 57, pp. 879–902, 2019.

[4] H. Liu, J. Zhong, C. Lee, S. W. Lee, and L. Lin, "A Comprehensive Review on Piezoelectric Energy Harvesting Technology: Materials, Mechanisms, and Applications," Appl. Phys. Rev., vol. 5, p. 041306, 2018.

[5] H. S. Kim, J. H. Kim, and J. Kim, "A Review of Piezoelectric Energy Harvesting Based on Vibration," Int. J. Precis. Eng. Manuf., vol. 12, pp. 1129–1141, 2011.

[6] T. Kumar, R. Kumar, V. S. Chauhan, and J. Twiefel, "Finite-Element Analysis of a Varying-Width Bistable Piezoelectric Energy Harvester," Energy Technol., vol. 3, pp. 1243–1249, 2015.

[7] M. Leinonen, J. Juuti, H. Jantunen, and J. Palosaari, "Energy Harvesting with a Bimorph Type Piezoelectric Diaphragm Multilayer Structure and Mechanically Induced Pre-stress," Energy Technol., vol. 4, pp. 620–624, 2016.

[8] J. Zhu et al., "Highly Reliable Real-time Self-powered Vibration Sensor Based on a Piezoelectric Nanogenerator," Energy Technol., vol. 6, pp. 781–789, 2018.

[9] J. Chen et al., "Biocompatible and Sustainable Power Supply for Self-Powered Wearable and Implantable Electronics Using III-Nitride Thin-Film-Based Flexible Piezoelectric Generator," Nano Energy, vol. 57, pp. 670–679, 2018.

[10] H. A. Sodano, D. J. Inman, and G. Park, "A Review of Power Harvesting from Vibration Using Piezoelectric Materials," Shock Vib. Dig., vol. 36, pp. 197–205, 2004.

[11] W. Liu et al., "Low Frequency Wide Bandwidth MEMS Energy Harvester Based on Spiral-Shaped PVDF Cantilever," Sci. China Technol. Sci., vol. 57, pp. 1068–1072, 2014.

[12] S. Shahab, S. Zhao, and A. Erturk, "Soft and Hard Piezoelectric Ceramics and Single Crystals for Random Vibration Energy Harvesting," Energy Technol., vol. 6, pp. 935–942, 2018.

[13] S. Ju and C. H. Ji, "Impact-Based Piezoelectric Vibration Energy Harvester," Appl. Energy, vol. 214, pp. 139–151, 2018.

[14] X. Jiang et al., "Piezoelectric Energy Harvesting from Traffic-Induced Pavement Vibrations," J. Renew. Sustain. Energy, vol. 6, p. 043110, 2014.

[15] N. Sezer and M. Koç, "A Comprehensive Review on the State-of-the-Art of Piezoelectric Energy Harvesting," Nano Energy, vol. 80, p. 105567, 2021.

[16] A. Proto, M. Penhaker, S. Conforto, and M. Schmid, "Nanogenerators for Human Body Energy Harvesting," Trends Biotechnol., vol. 35, pp. 610–624, 2017.

[17] S. A. Akkaya Oy, "A Piezoelectric Energy Harvesting from the Vibration of the Airflow around a Moving Vehicle," Int. Trans. Electr. Energy Syst., vol. 30, p. e12655, 2020.

[18] K. Uchino, "Piezoelectric Energy Harvesting Systems—Essentials to Successful Developments," Energy Technol., vol. 6, pp. 829–848, 2018.

[19] R. Li et al., "Harvesting Energy from Pavement Based on Piezoelectric Effects: Fabrication and Electric Properties of Piezoelectric Vibrator," J. Renew. Sustain. Energy, vol. 10, p. 054701, 2018.

[20] X. Wang et al., "An Energy Harvester for Low-Frequency Electrical Signals," Energy Technol., vol. 8, p. 2000114, 2020.
[21] T. V. Galchev, J. Mccullagh, R. L. Peterson, and K. Najafi, "Harvesting Traffic-Induced Vibrations for Structural Health Monitoring of Bridges," J. Micromech. Microeng., vol. 21, p. 104005, 2011.
[22] M. Amin Karami and D. J. Inman, "Powering Pacemakers from Heartbeat Vibrations Using Linear and Nonlinear Energy Harvesters," Appl. Phys. Lett., vol. 100, p. 042901, 2012.
[23] S. P. Beeby, M. J. Tudor, and N. White, "Energy Harvesting Vibration Sources for Microsystems Applications," Meas. Sci. Technol., vol. 17, p. R175, 2006.
[24] R. Vullers et al., "Micropower Energy Harvesting," Solid State Electron., vol. 53, pp. 684–693, 2009.
[25] Y. Tan, Y. Dong, and X. Wang, "Review of MEMS Electromagnetic Vibration Energy Harvester," J. Microelectromech. Syst., vol. 26, pp. 1–16, 2016.
[26] P. Pillatsch, E. M. Yeatman, and A. S. Holmes, "A Piezoelectric Frequency Up-Converting Energy Harvester with Rotating Proof Mass for Human Body Applications," Sens. Actuators A Phys., vol. 206, pp. 178–185, 2014.
[27] P. Miao et al., "MEMS Inertial Power Generators for Biomedical Applications," Microsyst. Technol., vol. 12, pp. 1079–1083, 2006.
[28] C. H. Wong and Z. Dahari, "Development of Vibration-Based Piezoelectric Raindrop Energy Harvesting System," J. Electron. Mater., vol. 46, pp. 1869–1882, 2017.
[29] Z. Zhang et al., "Design, Modelling and Practical Tests on a High-Voltage Kinetic Energy Harvesting (EH) System for a Renewable Road Tunnel Based on Linear Alternators," Appl. Energy, vol. 164, pp. 152–161, 2016.
[30] L. Zhen, Y. Wang, and S. Bai, "Generation Characteristics of Piezoelectric Vibrator Driven by Groove Cam: Simulation and Experimental Analysis," J. Renew. Sustain. Energy, vol. 8, p. 064701, 2016.
[31] P. Costa et al., "Recent Progress on Piezoelectric, Pyroelectric, and Magnetoelectric Polymer-Based Energy-Harvesting Devices," Energy Technol., vol. 7, p. 1800852, 2019.
[32] C. V. Karadag, S. Ertarla, N. Topaloglu, and A. F. Okyar, "Optimization of Beam Profiles for Improved Piezoelectric Energy Harvesting Efficiency," Struct. Multidiscip. Optim., vol. 63, pp. 631–643, 2020.
[33] G. Varade, L. Bhamare, H. Mehta, and N. Mitra, "Recent Progress in MEMS Based Acoustic Vector Sensor for Underwater Applications," in 2021 7th International Conference on Electrical, Electronics and Information Engineering (ICEEIE), Malang, Indonesia, pp. 307-312, 2021.